ELSEVIER

Sapphire (0 0 0 1) surface modifications induced by long-pulse 1054 nm laser irradiation

Sheng-Nian Luo [a,*], Pedro D. Peralta [b,1], Chi Ma [c], Dennis L. Paisley [a], Scott R. Greenfield [d], Eric N. Loomis [a]

[a] Physics Division, Los Alamos National Laboratory, Los Alamos, NM 87545, USA
[b] Materials Science and Technology Division, Los Alamos National Laboratory, Los Alamos, NM 87545, USA
[c] Division of Geological and Planetary Sciences, California Institute Technology, Pasadena, CA 91125, USA
[d] Chemistry Division, Los Alamos National Laboratory, Los Alamos, NM 87545, USA

Abstract

We have investigated modifications of sapphire (0 0 0 1) surface with and without coating, induced by a single laser pulse with a 1054 nm wavelength, 2.2 μs duration, 7.75 mm spot and energy of 20–110 J. A holographic optical element was used for smoothing the drive beam spatially, but it induced small hotspots which initiated damage on the uncoated and coated surfaces. The individual damage effects of hotspots became less pronounced at high fluences. Due to high temperature and elevated non-hydrostatic stresses upon laser irradiation, damage occurred as fracture, spallation, basal and rhombohedral twinning, melting, vitrification, the formation of nanocrystalline phases, and solid–solid phase transition. The extent of damage increased with laser fluences. The formation of regular linear patterns with three-fold symmetry ($\langle 1\,1\,\bar{2}\,0 \rangle$ directions) upon fracture was due to rhombohedral twinning. Nanocrystalline α-Al_2O_3 formed possibly from vapor deposition on the coated surface and manifested linear, triangular and spiral growth patterns. Glass and minor amounts of γ-Al_2O_3 also formed from rapid quenching of the melt on this side. The α- to γ-Al_2O_3 transition was observed on the uncoated surface in some partially spalled alumina, presumably caused by shearing. The nominal threshold for laser-induced damage is about 47 J cm^{-2} for these laser pulses, and it is about 94 J cm^{-2} at the hotspots.
© 2007 Elsevier B.V. All rights reserved.

Keywords: Sapphire; Laser irradiation; Spall; Fracture; Twinning; Nanocrystals

1. Introduction

Sapphire (α-Al_2O_3) is an important optical material [1] for its broad transmission spectrum from ultraviolet to visible and near-infrared (0.2–2 μm), high resistance to abrasion, thermal shock and particle impact due to its high strength, and high shock impedance (the product of density and shock wave speed). Thus, sapphire has been used widely as both windows and substrates in demanding environments such as dynamic shock wave experiments induced by intense laser illumination [2–4], to transmit probe or drive lasers and to produce and sustain high loading stress.

Extensive studies have been conducted to investigate damage and structural modifications in sapphire induced by various loading techniques ranging from femto- and nano-second lasers to conventional shock waves (e.g., gas guns) [5–15]. However, it has rarely been explored for long-laser pulses in the range of 100 ns to μs. For example, sapphire has been used as substrates in laser-driven flyer-plate shock wave experiments [2–4]. In such experiments, the uncoated sapphire surface transmits the drive laser, while the coated surface absorbs the laser to create inertially and mechanically confined plasma and vapors which launch the flyer plate. The thermal and mechanical damage of both surfaces upon intense laser irradiation could reduce the efficiency of converting laser energy into the kinetic energy of the flyer plate. Preserving the optical and mechanical integrity of sapphire is particularly important for achieving desired stress levels in such laser-driven shock wave experiments [2–4]. Thus, it is also of

---

technical relevance to examine laser-induced damage on both coated and uncoated surfaces. In order to achieve well defined one-dimensional shocks, the drive laser is often modulated spatially with a holographic optical element (HOE). While the original Gaussian-shaped beam is transformed into a bulk tophat shape, numerous hotspots may be created as a byproduct. As substrate damage is most likely initiated at hotspots, it is necessary to understand their individual and collective damage effects. Here we report our long-pulse laser ablation experiments on sapphire single crystals, investigating laser-induced damage on the coated and uncoated (0 0 0 1) surfaces, including fracture, spall, deformation, melting, vitrification, the formation of nanocrystalline phases, and solid–solid phase transition.

2. Experimental

The schematic setup of our long-pulse laser irradiation experiments is shown in Fig. 1. The target assembly was composed of a sapphire substrate coated with an ablative layer, and a confinement layer (Cu disk 0.1–0.5 mm thick), and located in a vacuum chamber (10^{-5} to 10^{-4} Torr). The ablative layer was vapor deposited on the substrate and composed of sequentially, 0.5 μm C, 0.5 μm Al, 0.5 μm Al_2O_3, and 5 μm Al on the top. Laser illumination on this absorbing layer induced a high temperature mixture of vapors and plasmas that were confined inertially and mechanically by the metal confinement layer at early stages, and its expansion created stress waves propagating into the substrate and the confinement layer. The confinement layer was separated and launched as a flyer plate at later stages. In some cases, a PMMA window was clamped to the assembly for sustained confinement since the confinement layer cannot be launched. Initial damage on the uncoated surface of the substrate (the laser entrance side) was due to its optical breakdown. Damaged areas on both surfaces also absorbed laser energy and contributed to heating coupled with elevated stresses. Temperature and stresses were then released

to ambient conditions, and the substrate was recovered for analysis.

In the case with a window clamped to the substrate, the confinement duration for the plasma/vapor mixture was substantially longer than the drive pulse duration. In the case without a PMMA window, the Cu confinement layer was separated from the substrate and launched as a flyer plate before the pulse ended. The confinement was reduced upon separation. This confinement reduction may be partially compensated by continued absorption of laser power into the plasma/vapor mixture. In both cases, the sapphire on the coated side could have been damaged before the pulse ended, and this area absorbed laser energy and induced further damage. In the former case, longer and higher loading was achieved compared to the latter case and to free ablation on the uncoated surface. (The confinement and stress level were considerably lower in free ablation.)

The cylindrical sapphire single crystals (CVI Laser, LLC) were 19.1 mm in diameter and 7.6 mm in thickness. Their (0 0 0 1) surfaces were optically finished. We adopted Kronberg's morphological indices [16] for indexing planes and directions in sapphire single crystal, and $c/a = 2.73$. The complex refraction index of sapphire $\tilde{n} = n + i\kappa$ with $n \approx 1.77$ and $\kappa \approx 0$ (transparency) at 1 μm. The transmission is dominated by reflection at two surfaces. The reflectivity $R = (1 - n)^2/(1 + n)^2 \approx 0.08$. Thus, the transmission is $(1 - R) \approx 0.92$ and $(1 - R)^2 \approx 0.85$ for the entrance (uncoated) and exit surfaces, respectively. However, the exit surface may be damaged quickly by the absorbing coating and the exact reflectivity and absorption then become unknown.

Our laser irradiation experiments were conducted at the Trident laser facility with a Nd:glass laser driver (fundamental wavelength 1054 nm), which employs a Nd:YLF master oscillator and a chain of Nd:phosphate glass rod and disk amplifiers in a conventional master oscillator, power amplifier (MOPA) architecture. The oscillator pulse is temporally shaped, amplified and delivered to target through an HOE. The temporal shape of the drive pulse can be Gaussian, ramping or other types. The full width at half maximum (FWHM) ranges from about 100 ns to 5 μs, and the total energy of a single pulse without relay loss is 10–500 J.

The laser power of the drive pulse as a function of time can be approximated as a Gaussian function:

$$P(t) = \frac{E_0}{\sqrt{2\pi}\sigma} \exp\left\{ -\frac{(t - t_0)^2}{2\sigma^2} \right\}. \tag{1}$$

Here t denotes time, and t_0 and σ are parameters. σ is related to FWHM as $\mathrm{FWHM} = 2\sqrt{2\ln 2}\sigma = 2.2$ μs. E_0 denotes pulse energy accounting for the optical relay loss (about 56%) but not the reflection at either surface. The irradiance follows as $I_r(t) = 4P(t)/\pi\phi^2$, where ϕ is the diameter (7.75 mm) of the drive laser spot. We define accumulative fluence as $F(t) = \int_{-\infty}^{t} I_r(t)\, dt$. Its value at the end of the pulse, $F_\infty = 4E_0/\pi\phi^2$, is normally used to determine the laser-induced damage threshold. However, the drive pulse durations were exceptionally long in our experiments and damage could
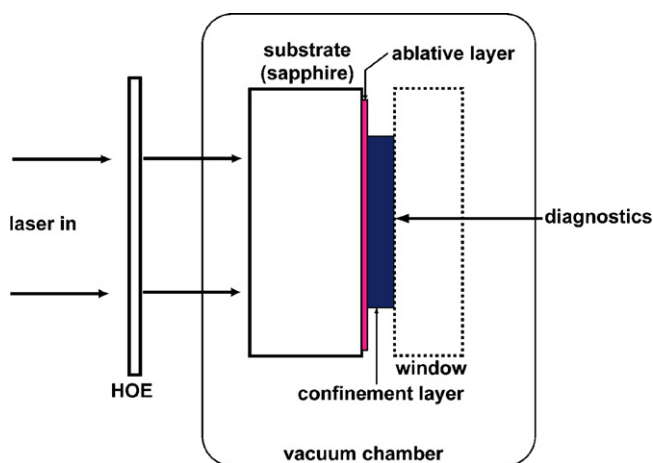

Fig. 1. Schematic of the experimental setup. HOE denotes holographic optical element. The ablative layer is vapor deposited on the substrate. A clamped window may be used for further confinement of plasma and vapor. The diagnostics include a point velocity interferometer.

Table 1
Summary of shots

Shot #[a]	E_0[b] (J)	max. I_r[b,c] (GW cm^{-2})	F_∞[b] (J cm^{-2})	Damage[d]
Without a window (flyer plate)				
19200	22	0.020	47	Negligible
19201	32	0.029	68	Minor
19218	45	0.041	95	Minor
19202	53	0.048	112	Minor
19217	69	0.063	146	Medium
19216	74	0.067	157	Medium
19215	75	0.068	159	Medium
19203	76	0.069	161	Medium
19204	92	0.084	195	Medium
With a clamped PMMA window (4 mm thick)				
19124	96	0.087	204	Severe
19125	108	0.098	229	Severe

[a] FWHM = 2.2 µs, $\sigma = 0.93$ µs and $\phi = 7.75$ mm.
[b] Defined for the drive pulse without reflection losses at the substrate. The values are reduced by 8% and 15% for the uncoated and coated surfaces, respectively.
[c] Defined at t_0, Eq. (1).
[d] Uncoated surface.

have well been induced before the pulse ended. Thus $F(t)$ at the instant of damage is more appropriate than F_∞. Unfortunately, we were not able to measure *in situ* the exact damage process, so F_∞ was adopted in our discussion. The pulse energy, irradiance and fluence can also be evaluated at the uncoated and coated surfaces. The reflection loss at these two surfaces with respect to the drive pulse was 8% and 15%, respectively. The following discussions refer to the drive pulse (Table 1).

The spatial profile of the original drive pulse was Gaussian, thus unsuitable for producing homogeneous planar stress profile in the confinement layer intended for dynamic materials experiments. We adopted a diffractive HOE for laser beam shaping, transforming the original bulk Gaussian shape into a tophat with small hotspots riding on it (blue dots in Fig. 2a). The hotspots were spaced at 95 µm on a square grid, all of which contained about 45% of the entire pulse energy. These hotspots had a Gaussian radius of 28 µm. The fluence at the hotspots was roughly four times higher than at other points on the tophat. Given the existence of hotspots, the fluence and irradiance defined above only represent average or nominal values, and the values at the hotspots are about two times higher. For convenience, our discussions below refer to the nominal values unless stated otherwise.

A point velocity interferometry system for any reflector (VISAR) [17] was used for time-resolved measurement of the particle velocity at the interface between the window (or free surface) and the confinement layer during laser ablation. The stress history of the ablation layer can then be deduced from such a measurement and known equations of state for the confinement layer (Cu) and the PMMA window (or free surface) [18], and details were omitted here. Examples of the particle velocity and corresponding stress histories are shown in Fig. 3.

The sapphire substrates were recovered. The coated and uncoated surfaces were then analyzed with optical and electron microscopic techniques including scanning electron microscopy (SEM) and electron back scattering diffraction (EBSD). One set of SEM/EBSD analysis was conducted with an FEI XL-30 scope at 10 kV as a compromise among reducing charging artifacts, obtaining better contrast from surface features and having enough interaction volume for reliable EBSD patterns. Some SEM imaging was conducted with a LEO 1550VP field
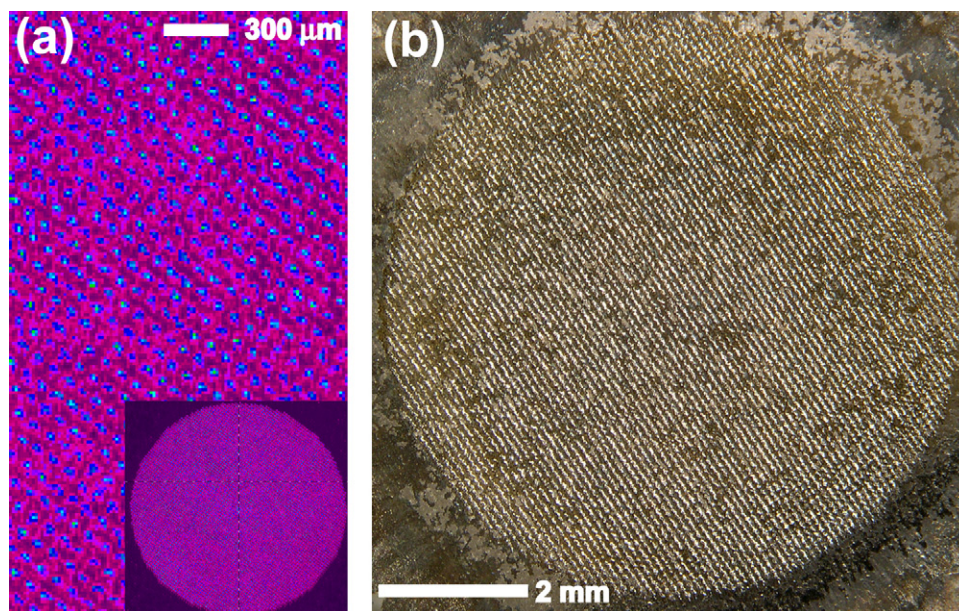

Fig. 2. (a) The drive beam profile (intensity distribution) as spatially modulated by HOE: the whole profile (inset: 7.75 mm in diameter) and an enlarged area for clarity. The blue dots denote hotspots forming a grid pattern (pin-cushion). The Gaussian radius of the hotspots is about 28 µm. The grid size is about 95 µm. (b) Optical image of the coated side (shot #19218, 95 J cm^{-2}): the damage pattern resembles the beam profile, and the grid width is about 94 µm. Similar pattern was also formed on the uncoated surface at sufficiently high fluences. (For interpretation of the references to color in this figure legend, the reader is referred to the web version of the article.)
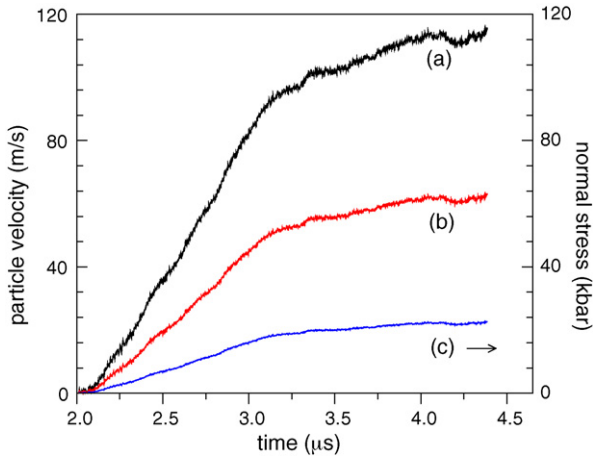
Fig. 3. Particle velocity at the PMMA window–Cu interface (a) and inside Cu (b), and the normal stress σ_1 within Cu (c); shot #19125, 229 J cm^{-2}. Curves (b) and (c) were calculated from (a) which was directly measured (1 kbar = 0.1 GPa).

emission microscope. EBSD analysis was also performed with an HKL EBSD system. In addition, a TSL-EDAX orientation imaging microscopy (OIM^{TM}) system was used. OIM^{TM} is based on automatic indexing of electron backscatter diffraction patterns, providing complete two-dimensional description of the crystallographic orientations in polycrystalline materials. No conducting coating was applied in these analyses.

3. Results and discussion

3.1. Estimate of stress and temperature

It is well known that the stress and temperature conditions on the coated and uncoated surfaces of the substrate can be extremely complicated during laser illumination and subsequent unloading to ambient conditions. This issue is still poorly understood in general and there are only some qualitative models proposed to date [11,15]. However, some estimates can be made as follows, using shot #19125 (229 J cm^{-2}) as an example.

The laser illuminated ablative layer induced stress waves propagating into both the substrate (the coated side) and the confinement layer (Cu). The deformation of Cu and sapphire can be regarded as uniaxial strain. We define the stress along the laser incident direction (i.e., [0 0 0 1] in sapphire) as σ_1 for both Cu and sapphire. σ_1 within Cu was deduced from the particle velocity at the PMMA–Cu interface (Fig. 3). Assuming stress equilibrium, σ_1 was equal for Cu, the ablated coating layer, and sapphire (the coated side). The peak value of σ_1 was about 2.2 GPa (Fig. 3) for sapphire, far below the Hugoniot elastic limit (HEL, σ_1 of 12–20 GPa) [19] obtained from shock wave loading along [0 0 0 1]. However, considerable heating during laser irradiation may reduce HEL for plasticity to occur. Note that this shot was conducted with a clamped PMMA window, so the Cu disk was not launched as a flyer plate. For flyer-plate experiments, σ_1 in sapphire cannot be determined definitely from the VISAR record because the exact instant when the flyer plate was separated from the substrate was unknown. A lower

bound of σ_1 was estimated as 0.5 GPa for such shots. For the uncoated surface upon breakdown, the stress induced by the vapor–plasma mixture is expected to be lower than the coated side due to a lack of confinement.

At such low stress conditions, compression-induced heating was negligible. Heating in sapphire was mostly due to heat conduction from the hot plasma and vapor, and to the absorption of laser (it was hotter on the coated side). Substrate temperature depends on thermal conductivity, heat capacity and absorption (α) [11]. α is a critical but time-dependent unknown parameter. If α is a constant regardless of the fluence and its time evolution, the temperature will scale linearly with fluences. This also indicates that the hotspot temperature could be two times higher than the bulk value. However, absorption of laser by damaged area increases with fluence and time once damage is initiated. Thus, meaningful calculations of the real temperature field is extremely difficult. However, estimation of temperature can be constrained by observations of recovered samples, e.g., melting and vaporization. The melting temperature for sapphire is 2051 K at ambient pressure. Thus, the temperature was at least 2000 K on the coated surface since melting was observed.

No measurement was made on the uncoated side for deducing its complicated stress history, and we only estimate the thermal stress (σ_{th}) here. Partial breakdown of a top thin layer may lead to its rapid heating to a temperature T_1 from ambient temperature T_0, creating a thermal gradient (heat conducting inward) and associated σ_{th}. (T_1 could be as high as 3300 K since a vapor-deposited nanocrystalline phase was observed for high fluences.) For a time scale of $t \sim 2$ μs, the diffusion distance is $\sqrt{4Dt} \sim 10$ μm, where the thermal diffusivity $D = 1.6 \times 10^{-5}$ m^2 s^{-1}[11]. The thermal gradient near the heated surface can be estimated as $(T_1 - T_0)(\pi Dt)^{-1/2}$, and the temperature drop over a distance (l) of 1 μm is $\Delta T \approx (l/\sqrt{\pi Dt})(T_1 - T_0) \approx 0.1(T_1 - T_0)$. For $T_1 - T_0 = 1000$ K, $\sigma_{th} = \alpha\Delta TE \sim 0.3$ GPa. Here the linear coefficient of thermal expansion $\alpha \approx 7 \times 10^{-6}$ K^{-1}, and Young's modulus $E = 460$ GPa along [0 0 0 1] [10]. σ_{th} may reach a stress level of 1 GPa over the whole diffusion distance, although the stress gradient was larger near the surface. Heat conduction also occurred on the coated side and it induced thermal stress as well. When a window was clamped to the substrate, the time scale and diffusion length would be longer.

At the end of the drive pulse, temperature decreased rapidly as heat conducted from a highly heated layer (heat source) further into the substrate. The quenching rate Q_q can be estimated as [20]:

$$Q_q = \frac{\kappa\Delta T}{C_p d^2}, \tag{2}$$

where κ is the thermal conductivity of the substrate (25 W m^{-1} K^{-1}[11]), ΔT the temperature difference between the source and background, and d and C_p are the thickness and heat capacity of the heat source, respectively. To estimate the order of magnitude of Q_q, we assume $d \sim 10$ μm, $\Delta T \sim 10^2$ to 10^3 K, and $C_p \sim 3$ J cm^{-3} K^{-1} [11]. Then Q_q was about 10^6 to

$10^7 \, \mathrm{K \, s^{-1}}$. However, we expect that Q_q was higher on the uncoated side than the coated side.

The sapphire substrate was under compression at early stages and possibly under tension later. A release wave may be initiated at free surfaces or due to a decaying compressional wave. Interaction of two opposing release waves may induce tensile stresses and spallation. The tensile (spall) strength of sapphire with minor compression heating is exceptionally large (20 GPa) [21]. However, as both surfaces were heated considerably during laser irradiation, its spall strength may be reduced sufficiently (e.g., to nearly zero at melting) for spallation to occur. Thermal stresses could also have contributed to fracture and spall.

Hotspots induced inhomogeneities in both stress and temperature fields. Their individual damage effects were dominated at low fluences. At sufficiently high fluences, the heterogeneities in the stress field, temperature field and damage were reduced considerably.

3.2. Fracture and spallation

SEM and optical examinations suggest that the dominating features of surface modifications were fracture (cracking) and spallation on both coated and uncoated surfaces (Figs. 2 and 4–6), and such damage increased with irradiance and fluence.

On the uncoated side, the damage induced by the lowest fluence (#19200, 47 J cm^{-2}, Table 1) was simply a small spot of about 80 μm in diameter within a 7.75 mm irradiated spot, representing a damage probability of 10^{-4} by area. Higher fluences up to about 110 J cm^{-2} induced a few scattered spots of damage with increasing number and size. A representative spot of damage is shown in Fig. 4(inset) with irregularly patterned fracture and fully and partially spalled regions. These
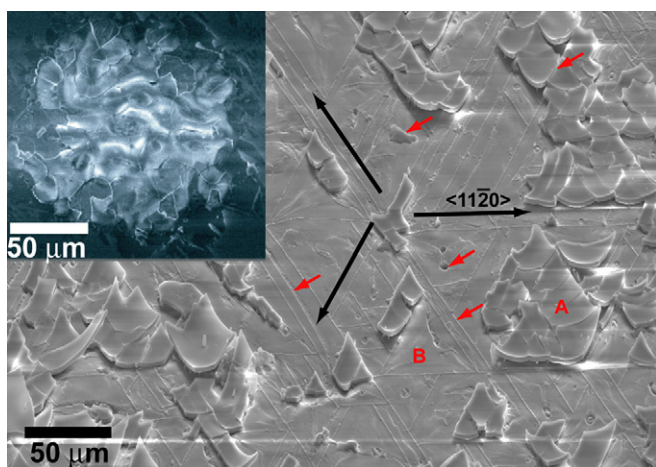

Fig. 5. Image quality map from an OIM scan of a region on the uncoated surface (shot #19124, 204 J cm^{-2}). Darker regions correspond to lower image quality.

damage spots were random. At fluences of 146–195 J cm^{-2}, the damage formed a grid pattern in one-to-one correspondence to the hotspot pattern as a result of HOE shaping (Fig. 2). Overall, a hotspot caused severe fracture and spallation around it. The damage was isolated and the areas enclosed by such spots manifested cracking with little spallation. At even higher fluences, the damage due to individual hotspots became much less isolated and more connected and homogenized (Fig. 4). And no clear correspondence between the damage and the hotspots can be identified.

Linear cracking mostly occurred along well defined crystallographic directions with three-fold symmetry, $\langle 1\,1\,\bar{2}\,0 \rangle$ (Figs. 4 and 5). The cracks may become curved and the symmetry may be reduced due to inhomogeneous stress and temperature conditions, e.g., at the localized damage spots for

Fig. 4. SEM imaging of an area on the uncoated surface, with a 70° tilt (shot #19124, 204 J cm^{-2}). The red arrows denote representative damage features, and black arrows, the orientation of the linear features (twinning). 'A' denotes the partially spalled top layer (flakes), and 'B', the exposed area after complete spallation of flakes. Inset: a damage spot on the uncoated surface at low fluences (#19218, 95 J cm^{-2}), showing fracture and spallation. (For interpretation of the references to color in this figure legend, the reader is referred to the web version of the article.)
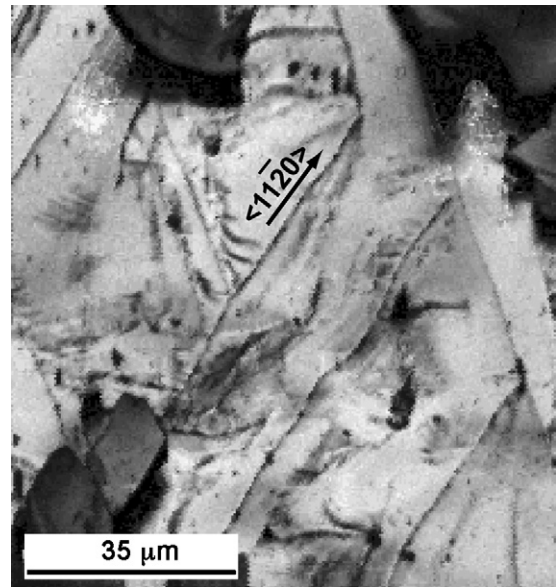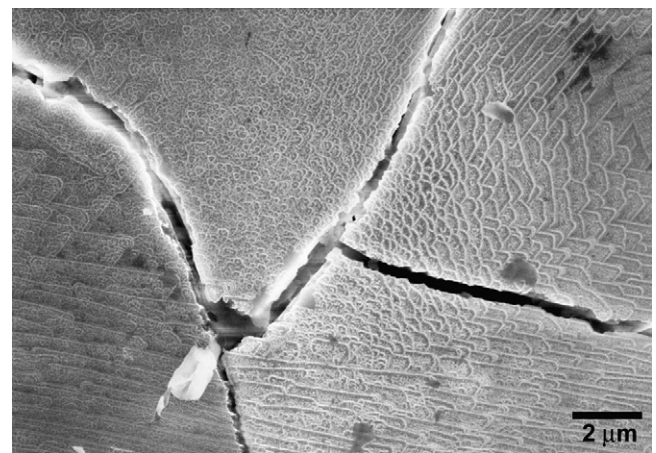

Fig. 6. SEM image showing the formation of cracks and nanocrystalline α-Al$_2$O$_3$ on the coated side (shot #19124, 204 J cm^{-2}). Nanocrystalline α-Al$_2$O$_3$ forms terraces with linear features and sharp corners.

low fluence shots (Fig. 4, inset). Cracking was possibly initiated from intersecting twins [22](see below) during compression and tension. The fully or partially spalled alumina (flakes) were formed via tension as the heating may have significantly reduced the spall strength. The thickness of the flakes was about 1.2 μm. Some flakes were curved upward due to residual stresses. The exposed surface was fairly flat, except for pronounced linear features (twinning) coinciding with crack directions and the edges of the flakes along $\langle 1\,1\,\bar{2}\,0\rangle$. These linear features were either parallel or intersected at 60° angles. The OIM image quality for the flakes was much poorer than the exposed surface (Fig. 5), indicating their significant deformation or distortion. A closer examination of these lines showed that they contained and were surrounded by ridges and other features typical of brittle fracture mechanisms such as cleavage (Fig. 4).

The coated surface is more susceptible to damage because of the absorbing coating and the confinement layer for longer, stronger and hotter loading. Therefore, considerable damage was induced even at the lowest fluence investigated (47 J cm^{-2}), which nonetheless caused only negligible damage on the uncoated surface. The main damage was cracking with some spallation at higher fluences (Fig. 6). Most cracks were curved, except some with linear features of three-fold symmetry similar to those on the uncoated side. The regular linear feature was less common and may be related to twinning. The irregular pattern may be associated with lateral tension (perpendicular to [0 0 0 1]) due to edge release waves or inhomogeneous thermal stresses. The flake thickness was about 3.3 μm, appreciably thicker than the uncoated side (1.2 μm, shot #19125, 229 J cm^{-2}). The flakes could have formed from encountering release waves, thermal stresses, or their combinations. The flake thickness seems to correlate better with the diffusion depth. The sustained confinement at the coated side may have induced thicker flakes but less spallation.

The hotspot effect was manifested on the coated surface even at low fluences: the optical image of the irradiated area (Fig. 2b) was similar to the hotspot pattern. (Similar damage pattern was observed on the uncoated surfaces at higher fluences.) The individual hotspot effects were homogenized at high fluences (Fig. 4).

3.3. Plasticity

Sapphire can deform plastically via twinning and slip. Basal twinning and dislocation slip have been observed for high strain rate shock wave loading [5–7], and rhombohedral twinning has been induced under compression at various temperatures [22–24]. Sapphire appeared to have undergone basal and rhombohedral twinning under elevated temperature and non-hydrostatic stresses in our experiments.

It is possible that the $\langle 1\,1\,\bar{2}\,0\rangle$ linear features (Figs. 4 and 5) are traces of twins. We thus conducted an EBSD scan to explore possible changes related to them. An EBSD scan of the region enclosed by these linear features and at points on one of the linear features did not reveal any changes possibly due to the small interaction volume since twins tend to be thin [23], but the pattern quality was reduced as expected for such fractured and spalled regions.

However, examining some areas beneath the spalled flakes using EBSD, we found patterns corresponding to α-Al$_2$O$_3$ but rotated with respect to the pristine substrate. A typical EBSD pattern from one of those regions is shown in Fig. 7, along with the pattern for the substrate. Rotation matrices defining the orientations for these two patterns were analyzed using the techniques presented by Kocks et al. [25] to obtain the misorientation angle between these two orientations as well as the axis of rotation common to both of them. The orientation relationship between a feature and a matrix (pristine substrate) can be used to elucidate whether or not the feature is actually a basal twin. The two rotation matrices are shown below:

$$\mathbf{R}_{\mathrm{matrix}} = \begin{bmatrix} 0.6377 & 0.7703 & -0.0041 \\ 0.7614 & -0.6295 & 0.1547 \\ 0.1166 & -0.1017 & -0.9880 \end{bmatrix}, \qquad (3)$$
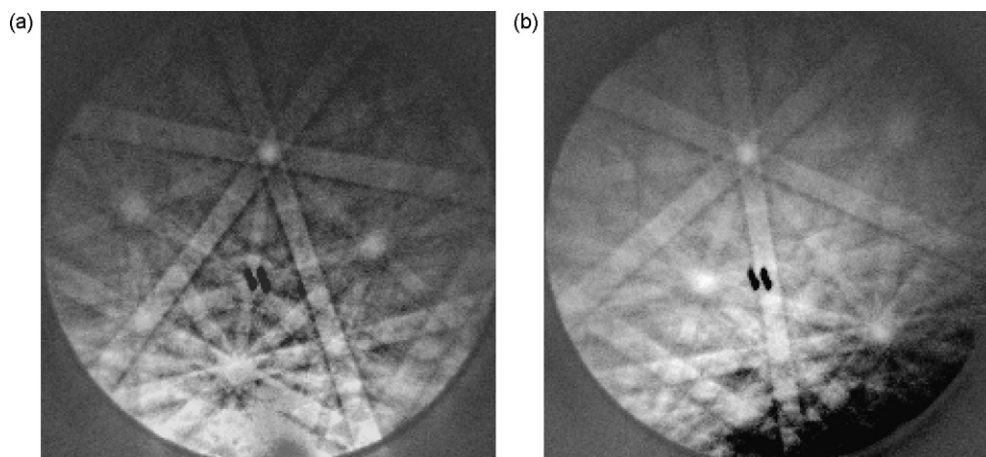

Fig. 7. Comparison of EBSD patterns on the uncoated surface from (a) original sapphire substrate, and (b) an exposed area beneath spalled flakes (shot #19124, 204 J cm^{-2}).

and

$$\mathbf{R}_{\text{feature}} = \begin{bmatrix} 0.9167 & 0.3859 & -0.1042 \\ -0.3982 & 0.9039 & -0.1557 \\ 0.0341 & 0.1842 & 0.9823 \end{bmatrix}. \qquad (4)$$

In these matrices, the crystallographic orientations parallel to the horizontal, vertical and normal directions are defined in an orthonormal system, and are given by the first, second and third row of the matrices, respectively. Both the matrix and the feature being analyzed have out of plane directions close to [0 0 0 1]. The misorientation angle θ is defined as

$$\cos\theta = \tfrac{1}{2}[\text{trace}(\mathbf{R}_{\text{matrix}}\mathbf{R}_{\text{feature}}^{\text{T}}) - 1]. \qquad (5)$$

The axis of rotation is given by the real eigenvector of the misorientation matrix $\mathbf{R}_{\text{matrix}}\mathbf{R}_{\text{feature}}^{\text{T}}$. In this case, the misorientation angle is about $178.6°$ and the rotation axis is only about $3°$ from $\langle 1\,0\,\bar{1}\,0 \rangle$. A basal twin in α-Al_2O_3 can be described as a rotation of $180°$ about $\langle 1\,0\,\bar{1}\,0 \rangle$ with a habit plane given by (0 0 0 1) [25]. These features were not common, but several of them were found under the flakes. It is likely that more twinned regions can be found under the surface of the sample, but the evidence indeed points to basal twinning as a deformation mode in these samples. Note that the out-of-plane directions are not exactly parallel to the [0 0 0 1] direction. A deviation of the shock direction from the normal to the basal plane has been invoked as one of the reasons for the presence of basal twinning in sapphire shocked along the [0 0 0 1] direction [5–7]. This is indeed consistent with the observations reported here.

The above analysis indicates the presence of small amounts of basal twinning. However, the $\langle 1\,1\,\bar{2}\,0 \rangle$ linear features may be caused by rhombohedral twinning with a $(1\,0\,\bar{1}\,2)$ twin plane and $\langle \bar{1}\,0\,1\,1 \rangle$ shear direction [22,24]. In uniaxial compression experiments by Schmid and Harris [22], the parallel lines (linear features) on the basal plane were attributed to the intersection of the rhombohedral twin planes and basal plane, and intersecting twins formed an angle of $60°$. These lines should follow $\langle 1\,1\,\bar{2}\,0 \rangle$, same as the linear features observed in our experiments.

In previous shock wave loading on single crystal sapphire using explosively driven flyer-plate experiments, plastic deformation was observed only above $\sigma_1 = 5$ GPa [6], due to the high elastic limit at such low temperatures and high strain rates. In such experiments, shock heating was negligible at such low stresses, in contrast to considerable heating of a thin layer in our experiment. Above 1000 K, the compression strength of sapphire along [0 0 0 1] decreases rapidly to about 2% of the room-temperature value (2 GPa), i.e., 0.04 GPa [22]. The Schmid factor for rhombohedral twinning is 0.452. Then the critical resolved shear stress required to initiate rhombohedral twinning is only about 0.02 GPa at such high temperatures [22]. To a first-order approximation, the resolved shear stress due to σ_1 before plasticity, was about 1 GPa on the coated side, and 0.14 GPa due to thermal stress on the uncoated side (shot #19125, 229 J cm^{-2}), assuming σ_1 of 2.2 and 0.3 GPa, respectively. Thus, rhombohedral twinning can be readily

initiated in our experiments if we do not consider the strain rate effect. Note in our experiments and previous impact experiments, strain rates were significantly higher (compared to such experiments as Schmid and Harris [22]), thus higher elastic limit is expected. Actually, the HEL for bulk plasticity is about 12–20 GPa in the latter experiments. Although the exact values of the critical resolved shear stress for rhombohedral twinning are unknown at high strain rates and high temperatures, the significant decrease of the compression strength as observed in the low-strain rate and high temperature experiments [22], strongly suggests that high temperatures in our experiments are the key reason for rhombohedral twinning, despite the lower stresses compared to previous impact experiments [5–7].

Our results show the presence of both basal and rhombohedral twinning. The fracture can be due to the intersection among rhombohedral twins [22,23] or the intersection of basal twins and rhombohedral twins [26]. The presence, or lack, of dislocation activity by itself cannot be deduced from the data collected, although twinning in sapphire can be attributed to dislocation glide. However, it is likely that there is dislocation activity as well. Future work using transmission electron microscopy may be performed to study this aspect of the deformation of these samples.

3.4. Phase transitions

Based on either a face-centered cubic (fcc) or hexagonal close-packed (hcp) arrangement of oxygen anions, numerous Al_2O_3 structures have been identified [27], including γ, η, θ, θ', θ'', δ and λ (fcc), and α, κ and χ (hcp) phases. At high pressures, it assumes the $Rh_2O_3(II)$ structure [28,29]. However, only the corundum (α-Al_2O_3) and $Rh_2O_3(II)$ structures are thermodynamically stable phases of Al_2O_3 solid, and the latter is stable up to about 96 GPa [29]. All other structures are only metastable transit phases synthesized from various precursors including melt [27]. In particular, the melt $\rightarrow \gamma \rightarrow \delta$, $\theta \rightarrow \alpha$ crystallization sequence and the vapor $\rightarrow \kappa \rightarrow \alpha$ deposition sequence (chemical vapor deposition) have been identified [27,30]. Elevated stress or strain (e.g., shearing atomic planes [27]) may also induce transformation from one to another, for example, $\gamma \leftrightarrow \alpha$ during high pressure sintering of nanocrystalline alumina [8]. Our laser irradiation experiments involved both elevated temperature and stresses, and subsequent (rapid) unloading to ambient conditions. Consequently, we observed vaporization, melting, vitrification, nanocrystalline α- and δ-Al_2O_3, and α–δ transition on the coated or uncoated surface (Figs. 6 and 8–10). The $Rh_2O_3(II)$ phase was not observed, due to the low pressure in our experiments.

We examined the coated surface using SEM and EBSD, and found scattered amorphous areas and nanovoids (Fig. 8). This indicates the occurrence of melting followed by rapid quenching typical for laser illumination, as well as non-uniform temperature and stress fields at small length scales. The initial melted layer was thin. While it is highly desirable to synthesize pure bulk Al_2O_3 glass for its superior mechanical, optical and chemical properties, Al_2O_3 alone is extremely difficult to form pure bulk glass [31]. The formation of a

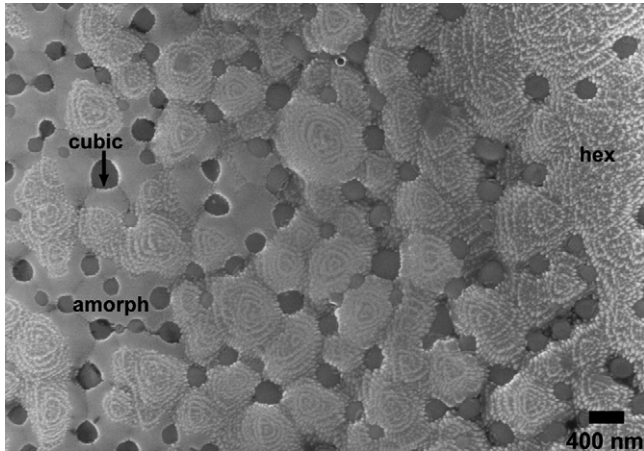Fig. 8. SEM image showing the formation of nanovoids, nanocrystalline α- and γ-Al$_2$O$_3$, and amorphous glass on the coated side (shot #19125, 229 J cm^{-2}). The cubic γ-phase is scattered near the walls of nanovoids, and the hexagonal α-phase forms spiral and triangular patterns.

limited amount of pure Al$_2$O$_3$ glass in our ablation experiments can certainly be attributed to the high quenching rate (about 10^6 to 10^7 K s^{-1}). Similarly, glass formed under 200 fs laser ablation of uncoated sapphire surface [15], but was almost absent on the uncoated surface in our experiments with much lower intensity.

The formation of nanocrystalline α- and γ-Al$_2$O$_3$ ($\sim$ 20 nm) was evident from the SEM and EBSD patterns (Figs. 6, 8 and 9), also due to fast quenching rates. A small amount of γ-Al$_2$O$_3$ was located near the edges of the nanovoids (Fig. 8), and α-Al$_2$O$_3$ (sapphire) was dominant. The orientation of nanocrystalline α-Al$_2$O$_3$ is also [0 0 0 1], following the substrate to reduce free energy. Interestingly, the nm grains of α-Al$_2$O$_3$ form linear, triangular and spiral patterns. Both vaporization and melting have occurred in our experiments, and the nanocrystalline phases may have formed from supersaturated vapor or melt, or both. The existence of γ-Al$_2$O$_3$ appears to favor its formation from melt, consistent with the crystallization sequence observed previously [27,30]. Nonetheless, the spiral pattern formed by nanocrystalline α-Al$_2$O$_3$ can be better explained by growth from vapor (see below), and κ-Al$_2$O$_3$ was not detected possibly because of the rapid κ to α transformation kinetics in our experiments.

The nm grains of α-Al$_2$O$_3$ formed spiral patterns with various curvatures (linear, triangular and circular). Similar patterns have been observed for hematite (α-Fe$_2$O$_3$, an isomorph of α-Al$_2$O$_3$) formed from the reaction of iron chloride gas and water [32]. The morphology of spiral pattern has been related to screw dislocations upon growth from a vapor or solution [33], or from a eutectic (e.g., Zn–Mg alloy) due to growth anisotropy [34]. (The latter is not our case.) The exact
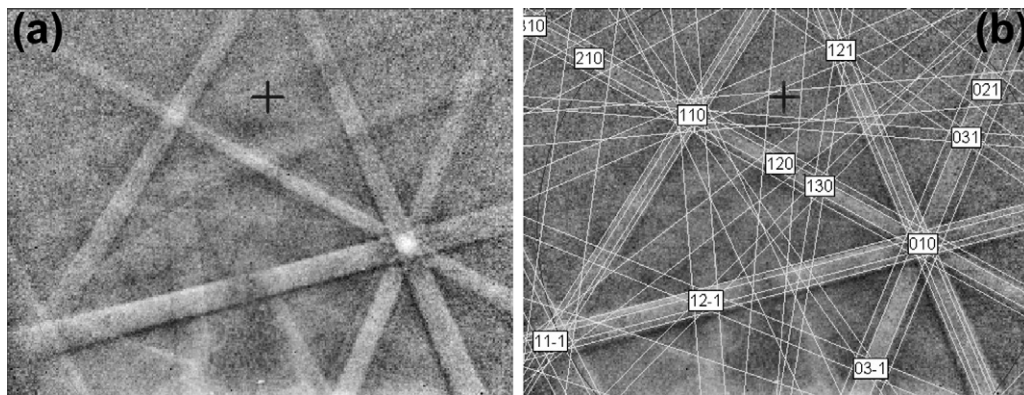

Fig. 9. (a) EBSD pattern from a nanocrystalline phase on the coated surface, and (b) its indexing as γ-Al$_2$O$_3$ (shot #19125, 229 J cm^{-2}).
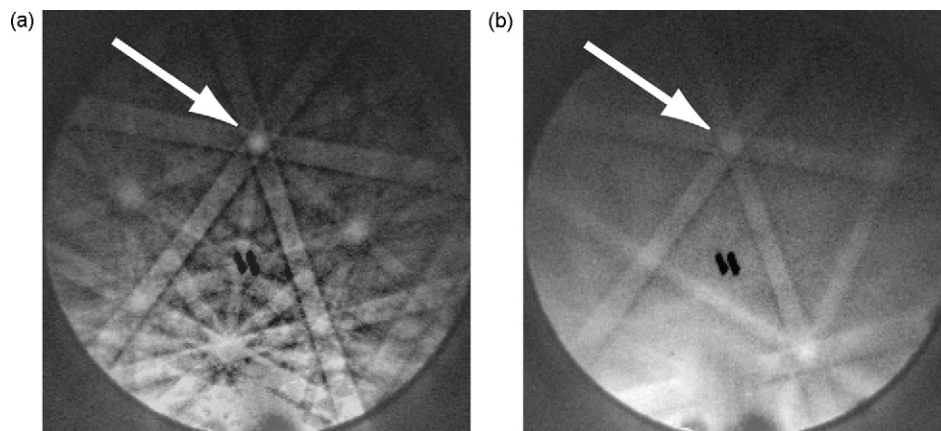

Fig. 10. EBSD patterns on the uncoated surface (shot #19124, 204 J cm^{-2}) from (a) an exposed area (underneath spalled flakes) remaining as α-Al$_2$O$_3$, and (b) a surface flake that transformed to γ-Al$_2$O$_3$. The arrow indicates a pole possibly common for the two patterns.

shape of the pattern depends on the extent of supersaturation in a vapor–solid system, the local temperature and stress fields as well as the crystallographic symmetry of the growth plane, e.g., the triangular pattern can be naturally related to the three-fold symmetry of the (0 0 0 1) surface. Upon laser irradiation, a mixture of vapor and plasma was induced on the coated surface, and the high temperature-induced vaporization and melting of α-Al_2O_3. Christian [35] related the curvature to the advance velocity of a step formed from a dislocation, and the rate of evaporation. An initially straight step may wind up into a spirally terraced hill (Fig. 8). However, early stages of the spiral growth were quenched as linearly or triangularly terraced hill (Fig. 6), possibly due to locally different supersaturation, stress and temperature conditions.

On the uncoated surface, nanocrystalline α-Al_2O_3 was also found for shots with sufficient fluences, mostly manifested as an extremely thin layer on partially spalled flakes. The nanocrystalline grains may also have formed from vapor deposition during local optical breakdowns, but were scattered without developing into any linear or spiral patterns as seen on the coated side. This is possibly due to the limited amount of vapor and confinement duration.

Besides vapor-condensed nanocrystalline α-Al_2O_3, γ-Al_2O_3 was identified from the EBSD pattern (Fig. 10) on partially spalled flakes $\sim 1\ \mu m$ thick. Such a thickness ruled out its formation from melt. A quantitative measure of the reliability of indexing a measured pattern is the confidence index (CI), ranging from 0 and 1 (perfect match). In this case, CI was 0.05 and 0.8 if the flake pattern was indexed as α- and γ-Al_2O_3, respectively, thus indicating the α- to γ-Al_2O_3 transition. The poles marked in Fig. 10 correspond to the basal plane for the substrate and to a $\{1\,1\,1\}$ plane in the cubic structure of the flake, and seem to be common to these two patterns. This suggests an orientation relationship between them: these two corresponding compact planes are parallel to one another as commonly observed in many materials. The patterns from the flakes had a couple of variants, with the $\{1\,1\,1\}$ pole always at the same position, but with different locations for the $\{0\,0\,1\}$ pole. The curvature of the flakes and the lower quality of their EBSD patterns suggest the presence of pronounced residual stresses. The lattice parameter a of γ-Al_2O_3 (0.79 nm) is larger than $a = 0.475$ nm for α-Al_2O_3 [27], so additional stresses may result from the lattice mismatch. One explanation to the formation of γ-Al_2O_3 is shearing of atoms during fracture and spallation processes, similar to the $\alpha \leftrightarrow \gamma$ transformation during high-pressure sintering of nanocrystalline alumina [8,27]. (Hotspots may have contributed to local shearing.) A possible atomistic synchro-shear mechanism [27,36] for the $\gamma \rightarrow \alpha$ transitions was proposed for Fe_2O_3, and it may also be valid for its inverse transition.

3.5. Laser-induced damage threshold

Both the uncoated and coated surfaces underwent different degrees of damage, and the damage on the coated side made it extremely difficult to quantify consistently the damage probability on the uncoated side in particular for high fluences.

The laser-induced damage threshold (LIDT) refers to the uncoated surface. We thus classified the damage qualitatively into four categories: negligible, minor, medium, and severe (Table 1). For the lowest fluence shot (47 J cm^{-2}, #19200), the damage probability was about 10^{-4} and thus negligible; damage progressed from negligible, minor and medium to severe with increasing fluences (and irradiances). These results suggest that the nominal value of LIDT is about 47 J cm^{-2}, or 2×10^7 W cm^{-2} for 7.75 mm spot, 2.2 μs duration, and 1054 nm wavelength. The value is substantially higher (~ 94 J cm^{-2}) at the hotspots.

Previously, the damage probability as a function of irradiance was investigated by Martin et al. [9] using Nd:YAG laser (1064 nm) pulses of 7 ns duration and 30 μm spot size. Extrapolating their curve to zero probability yields an LIDT of about 4×10^9 W cm^{-2}, or 30 J cm^{-2}, comparable to the nominal value of 47 J cm^{-2} for sapphire (0 0 0 1) surface in our experiments.

Three main classes of mechanism may account for laser-induced damage to optical materials: thermal processes, dielectric processes and multiphoton ionization [11], and all induce local heating and stresses. Multiphoton ionization is related to extremely high laser intensity as in sub-ps and fs irradiation, and is irrelevant here. The experiments by Martin et al. [9] attributed the breakdown to dielectric processes. As sapphire is transparent near 1 μm wavelength, the initial damage in our experiments may also be due to dielectric breakdown, but the thermal processes may well contribute to the damage at later stages. Further investigations in the future are necessary to reveal its exact nature.

4. Conclusion

We have investigated the modifications on sapphire (0 0 0 1) surfaces with and without ablative coating under dynamic loading induced by long pulse (2.2 μs) laser irradiation. The damage includes fracture, spallation, twinning (basal and rhombohedral), melting, vitrification, the formation of nanocrystalline α- and γ-Al_2O_3, and α- to γ-phase transition. Fracture was possibly initiated with rhombohedral twinning which was manifested as linear features of three-fold symmetry. Nanocrystalline γ-phase and glass formed from melt on the coated side via rapid quenching, while nanocrystalline α-phase likely formed from deposition and showed linear, triangular and spiral growth patterns. The γ-phase was observed in partially spalled flakes on the uncoated side, possibly due to local shearing. Individual hotspots induced localized damage at low fluences, but they acted collectively and the damage became more homogenized at high fluences.

Damage on both coated and uncoated surfaces of sapphire may affect adversely its role as a laser transmitting and vapor/plasma confining medium in laser-driven shock wave experiments, e.g., laser-launched flyer-plate loading. The nominal value of the threshold for laser-induced damage on the optically finished (0 0 0 1) surface without coating is about 47 J cm^{-2} for 2.2 μs, 1054 nm and 7.75 mm laser pulse. This value is comparable to that for ns pulses. However, the threshold for

such long-pulse laser irradiation is substantially higher ($\sim 94\,\mathrm{J\,cm^{-2}}$) if we consider the small hotspots introduced by the holographic optical element. While the absorbing coating is highly desirable at the initial stage of laser irradiation, it may induce substantial damages to sapphire thereafter even at low fluences. Such damage reduces further absorption of laser energy and thus its conversion efficiency as well as sapphire's strength and confining effect. Optical elimination or reduction of such hotspots would greatly improve the performance of sapphire as a substrate or window during intense laser irradiation.

Acknowledgements

References

[1] M. Fox, Optical Properties of Solids, Oxford University Press, New York, 2001.

[2] D.L. Paisley, R.H. Warnes, R.A. Kopp, in: S.C. Schmidt, R.D. Dick, J.W. Forbes, D.G. Tasker (Eds.), Shock Compression of Condensed Matter—1991, North-Holland, Amsterdam, 1992, p. 825.

[3] S.N. Luo, D.C. Swift, T.E. Tierney IV, D.L. Paisley, G.A. Kyrala, R.P. Johnson, A.A. Hauer, O. Tschauner, P.D. Asimow, High Pressure Res. 24 (2004) 409.

[4] D.C. Swift, J.G. Niemczura, D.L. Paisley, R.P. Johnson, S.N. Luo, T.E. Tierney IV, Rev. Sci. Instrum. 76 (2005) 093907.

[5] Y. Wang, D.E. Mikkola, Mater. Sci. Eng. A 148 (1991) 25.

[6] Y. Wang, D.E. Mikkola, J. Am. Ceram. Soc. 75 (1992) 3252.

[7] S.-J. Chen, D.G. Howitt, Phil. Mag. 78 (1998) 765.

[8] S.-C. Liao, Y.-J. Chen, B.H. Kear, W.E. Mayo, NanoStruct. Mater. 10 (1998) 1063.

[9] P. Martin, A. Moroño, E.R. Hodgson, J. Nucl. Mater. 283–287 (2000) 894.

[10] A.G. Lanin, E.L. Muravin, V.P. Popov, V.T. Turchin, J. Eur. Ceram. Soc. 23 (2003) 455.

[11] R.M. Wood, Laser-induced Damage of Optical Materials, Institute of Physics Publishing, Bristol, 2003.

[12] D.C. Harris, O. Esquivel, P.D. Chaffee, I. Anteby, R. Ifergan, M. Pinkas, A. Horowitz, H. Lotem, T.M. Regan, J.J. Mecholsky Jr., Proc. SPIE 5078 (2003) 61.

[13] I.H. Chowdhury, A.Q. Wu, X. Xu, A.M. Weiner, Appl. Phys. A 81 (2005) 1627.

[14] J.A. Randi, J.C. Lambropoulos, S.D. Jacobs, Appl. Opt. 44 (2005) 2241.

[15] E.G. Gamaly, S. Juodkazis, K. Nishimura, H. Misawa, B. Luther-Davies, Phys. Rev. B 73 (2006) 214101.

[16] M.L. Kronberg, Acta Metall. 5 (1957) 507.

[17] L.M. Barker, R.E. Hollenbach, J. Appl. Phys. 43 (1972) 4669.

[18] R.G. McQueen, S.P. Marsh, J.W. Taylor, J.N. Fritz, W.J. Carter, in: R. Kinslow (Ed.), High Velocity Impact Phenomena, Academic, New York, 1971, p. 314.

[19] L.M. Barker, R.E. Hollenbach, J. Appl. Phys. 41 (1970) 4209.

[20] K.S. Seol, H. Hiramatsu, Y. Ohki, I.-H. Choi, Y.-T. Kim, J. Mater. Res. 16 (2001) 1883.

[21] G.I. Kanel, S.V. Razorenov, A.V. Utkin, K. Baumung, H.U. Karow, V. Licht, in: S.C. Schmidt, J.W. Shaner, G.A. Samara, M. Ross (Eds.), High-pressure Science and Technology—1993, vol. 309, AIP Conference Proceedings, 1994, p. 1043.

[22] F. Schmid, D.C. Harris, J. Am. Ceram. Soc. 81 (1998) 885.

[23] A.H. Heuer, Phil. Mag. 13 (1966) 379.

[24] R.L. Bertolotti, W.D. Scott, J. Am. Ceram. Soc. 54 (1971) 286.

[25] U.F. Kocks, C.N. Tomé, H.-R. Wenk, Texture and Anisotropy, Cambridge University Press, 1998.

[26] K.P.D. Lagerlöf, A.H. Heuer, J. Castaing, J.P. Rivière, T.E. Mitchell, J. Am. Ceram. Soc. 77 (1994) 385.

[27] I. Levin, D. Brandon, J. Am. Ceram. Soc. 81 (1998) 1995.

[28] R.D. Shannon, C.T. Prewitt, J. Solid State Chem. 2 (1990) 134.

[29] J.F. Lin, O. Degtyareva, C.T. Prewitt, P. Dera, N. Sata, E. Gregoryanz, H.K. Mao, R.J. Hemley, Nat. Mater. 3 (2004) 389.

[30] V. Jayaram, C.G. Levi, Acta Metall. 37 (1989) 569.

[31] A. Rosenflanz, M. Frey, B. Endres, T. Anderson, E. Richards, C. Schardt, Nature 430 (2004) 761.

[32] I. Sunagawa, Am. Mineral. 47 (1962) 1139.

[33] W.K. Burton, N. Cabrera, F.C. Frank, Phil. Trans. R. Soc., London Ser. A 243 (1951) 299.

[34] B. Chalmers, Principles of Solidification, John Wiley & Sons, New York, 1964.

[35] J.W. Christian, The Theory of Transformation in Metals and Alloys, Pergaman, New York, 1965.

[36] S. Kachi, K. Momiyama, S. Shimuzu, J. Phys. Soc. Jpn. 18 (1963) 106.